



## Implicit hydromechanical representation of fractures using a continuum approach

Iman Vaezi<sup>a,b,c,\*</sup>, Francesco Parisio<sup>a,b,c</sup>, Keita Yoshioka<sup>d</sup>, Andres Alcolea<sup>e</sup>, Peter Meier<sup>e</sup>, Jesús Carrera<sup>b,c</sup>, Sebastià Olivella<sup>f</sup>, Víctor Vilarrasa<sup>a,\*\*</sup>

<sup>a</sup> Global Change Research Group (GCRG), IMEDEA, CSIC-UIB, Esporles, Spain

<sup>b</sup> Institute of Environmental Assessment and Water Research (IDAEA), Spanish National Research Council (CSIC), Barcelona, Spain

<sup>c</sup> Associated Unit: Hydrogeology Group UPC-CSIC, Barcelona, Spain

<sup>d</sup> Department Geoenergy, Montanuniversität Leoben, Austria

<sup>e</sup> Geo-Energie Suisse AG, Zürich, Switzerland

<sup>f</sup> Dept. of Civil and Environmental Engineering, Technical University of Catalonia (UPC-BarcelonaTech), Barcelona, Spain

### ARTICLE INFO

#### Keywords:

Equivalent fracture layer  
Fracture implicit representation  
Embedded model  
Fracture variable permeability  
Hydraulic stimulation of fractures

### ABSTRACT

Fractures control fluid flow, solute transport, and mechanical deformation in crystalline media. They can be modeled numerically either explicitly or implicitly via an equivalent continuum. The implicit framework implies lower computational cost and complexity. However, upscaling heterogeneous fracture properties for its implicit representation as an equivalent fracture layer remains an open question. In this study, we propose an approach, the Equivalent Fracture Layer (EFL), for the implicit representation of fractures surrounded by low-permeability rock matrix to accurately simulate hydromechanical coupled processes. The approach assimilates fractures as equivalent continua with a manageable scale ( $\gg 1 \mu\text{m}$ ) that facilitates spatial discretization, even for large-scale models including multiple fractures. Simulation results demonstrate that a relatively thick equivalent continuum layer (in the order of cm) can represent a fracture (with aperture in the order of  $\mu\text{m}$ ) and accurately reproduce the hydromechanical behavior (i.e., fluid flow and deformation/stress behavior). There is an upper bound restriction due to the Young's modulus because the equivalent fracture layer should have a lower Young's modulus than that of the surrounding matrix. To validate the approach, we model a hydraulic stimulation carried out at the Bedretto Underground Laboratory for Geosciences and Geoenergies in Switzerland by comparing numerical results against measured data. The method further improves the ability and simplicity of continuum methods to represent fractures in fractured media.

### 1. Introduction

Fractures are abundant in geological media. Either natural or engineered, fractures provide conductive pathways for mass and energy transport, supplying opportunities for exploitation of georesources, but also potential challenges for geo-engineering applications.<sup>1</sup> For example, in Enhanced Geothermal Systems (EGS) or water resource exploration in fractured geological media, fractures are the principal pathways for productivity.<sup>2</sup> In contrast, permeability of fractures (if present) should be as low as possible in host rocks for nuclear waste disposal<sup>3</sup> or cap rocks for geologic carbon storage.<sup>4,5</sup> In geo-engineering applications, fractured porous media behave under complex and fully

coupled (thermo-)hydromechanical processes. For instance, fractures intersected by or in the vicinity of the injection well may open as a result of pore pressure build-up causing permeability to increase, thus attenuating pressure build-up. Quantifying the dependence of fracture transmissivity on its aperture was the subject of some debate until Tsang (1992)<sup>6</sup> settled it by distinguishing between hydraulic (cubic law, approximately the geometric mean aperture), mass balance (mean aperture) and viscous dissipation apertures as the equivalent apertures of a parallel plate fracture with the same flow, transport, and energy dissipation as the actual fracture with spatially variable aperture. The distinction is adequate for coupled problem and support using the cubic law, which has proven adequate for hard rocks.<sup>7,8</sup> This law implies a

\* Corresponding author. Now at Department of Earth Sciences, Uppsala University, Uppsala, Sweden.

\*\* Corresponding author. Global Change Research Group (GCRG), IMEDEA, CSIC-UIB, Esporles, Spain.

E-mail addresses: [iman.vaezi@geo.uu.se](mailto:iman.vaezi@geo.uu.se) (I. Vaezi), [victor.vilarrasa@csic.es](mailto:victor.vilarrasa@csic.es) (V. Vilarrasa).

<https://doi.org/10.1016/j.ijmms.2024.105916>

Received 29 November 2023; Received in revised form 9 July 2024; Accepted 14 September 2024

Available online 19 September 2024

1365-1609/© 2024 The Authors. Published by Elsevier Ltd. This is an open access article under the CC BY-NC-ND license (<http://creativecommons.org/licenses/by-nc-nd/4.0/>).

strong coupling of fluid flow and geomechanical response of the fractured media to fluid injection/production. The coupling may be further complicated by thermal effects caused by, e.g., the injection of cold water into a hot system, which not only contracts the rock but also modifies the density and viscosity of the fluid, and therefore, e. g., hydraulic conductivity.<sup>9</sup> The meaningful modeling of strongly coupled processes demands a cost-effective simplified yet accurate representation of the fractured medium.

The highly heterogeneous nature of fractured media, including complex networks of heterogeneous fractures,<sup>10</sup> poses challenges to modeling approaches and calls for adequate representations of both matrix and fractures. One of the main challenges is to define and measure model parameters that allow the continuum scale modeling of scenarios in which fractures are either treated explicitly or considered implicitly within the porous medium itself. Explicit modeling comprises, amongst others, techniques such as (1) Discrete Fracture Matrix (DFM), attempting to strike a balance between loss of accuracy by upscaling and geometric complexity,<sup>11–13</sup> (2) Discrete Fracture Network (DFN), in which all fluid is assumed to be contained within the fracture network and the matrix is considered impermeable,<sup>14–16</sup> and (3) Conduits (channels) Networks (CN) that represent fractured media as a network of 1D connected pipe-like elements forming a series of channels for fluid flow.<sup>17,18</sup> In a porous medium, the secondary permeability offered by a conductive fracture may yield an overall effective permeability much greater than the primary permeability provided by the connected pores. As a result, flow occurs mainly along fractures and commonly leads to the assumption that the rock surrounding fractures is impermeable.<sup>19</sup> However, this assumption generally may lead to inaccurate predictions of pressure changes. Instead, accounting for the flux between fractures and rock matrix (so-called leak-off) improves predictions.<sup>20</sup>

Both explicit and implicit approaches present advantages and disadvantages. Explicit approaches are simple and render enhanced accuracy in the representation of fractures. However, they entail complex geometries and high computational costs.<sup>21,22</sup> The conventional implicit approach, called the continuum method, includes both fractures and matrix in an equivalent porous medium. Transforming discrete fractures into continuum representations requires upscaling.<sup>23</sup> Upscaling can be performed analytically or numerically. Analytical approaches<sup>24,25</sup> are generally based on geometry and/or flow features. Geometry-based upscaling approaches superimpose a grid onto the fracture network in which the corresponding fracture hydraulic conductivity (actually, any given property) is mapped on the grid formed by the intersections between fractures and the boundaries of the grid cells.<sup>26,27</sup> In flow-based upscaling, local steady-state solutions to the Laplace problem are usually employed to back-calculate effective permeabilities using Darcy's law.<sup>28,29</sup> In numerical-based methods, representative sub-grid scale DFN simulations can be used to obtain upscaled relationships including elements of the permeability tensor.<sup>30,31</sup>

The most common implicit numerical approaches include Equivalent Porous Medium (EPM, also known as the single-continuum approach), Stochastic Continuum (SC), and Dual Continuum Medium (DCM). If fractures are not well connected, the EPM method may be employed to define grid block-scale effective properties describing the behavior of the entire fractured rock mass.<sup>32</sup> There are several flow-based upscaling procedures such as the numerical upscaling proposed by Durlofsky (1991)<sup>28</sup> where equivalent grid-block permeabilities are computed by solving the fine scale pressure diffusion equation using effective medium theory representing fractures as thin ellipsoids embedded in a matrix,<sup>33,34</sup> and aggregation-based method.<sup>35</sup> However, there is no separation of the characteristic lengths in the fractures and in the matrix. Hence, upscaling to the average characteristics often leads to low model accuracy, even from the conceptual standpoint. For example, the secondary permeability provided by conductive fractures often yields an average effective permeability several orders of magnitude larger than the primary permeability of connected pores in the matrix, which leads to a different and generally more clustered pore pressure distribution

through the equivalent porous medium than the expected one.<sup>36</sup> Therefore, EPM approaches fail to deliver reliable solutions whenever fracture spacing is in the order of the reservoir characteristic length.<sup>36</sup>

SC approaches aim to develop equally-likely heterogeneous continua with stochastic representations of effective properties based on actual properties of the underlying fracture network.<sup>37</sup> The double or multi-continuum medium (DCM) approach is a preferable option among implicit approaches due to the more accurate representation of the embedding matrix. However, unconnected fractures can still communicate via the matrix (whose permeability is considered), making it difficult to identify hydraulic backbones (the dominating high transmissive structures).<sup>38</sup> In the presence of considerable matrix permeability, dual-permeability and dual-porosity models are advantageous as they represent fractures and matrix as separate continua that interact with each other through transfer functions. Dual-permeability models permit flow between matrix blocks, while dual-porosity models consider no communication between matrix blocks.<sup>39,40</sup> Fig. 1 shows a schematic of aforementioned methods and their relatively approximate accuracy versus each other and against the “true” fractured porous medium that is not possible to be fully characterized at all length scales.<sup>41</sup>

We introduce another implicit approach treating fractures as continuum layers, adjacent to the porous matrix, which are represented individually. This approach, termed Equivalent Fracture Layer (EFL), has the advantages of implicit (moderate computational cost), while displaying an accuracy similar to that of explicit methods (Fig. 1). However, the question of how to choose the assigned properties of the continuum-equivalent individual fracture models to reproduce the behavior of discrete fractures remains open. Property assignment is a non-trivial problem aggravated by the large differences between fracture aperture (usually  $\mu\text{m}$  to  $\text{mm}$ ) and reservoir characteristic length (generally  $\text{m}$  to  $\text{hm}$ ),<sup>42,43</sup> which leads to a negligible fracture volume compared with the volume of the surrounding medium.<sup>44</sup> In fact, the lower-dimensional nature of fractures with an extreme area-aperture ratio poses a great challenge to numerical simulations<sup>16,45</sup> using either implicit or explicit representations of fractures.<sup>46,47</sup>

Continuum methods are increasingly being combined with discrete

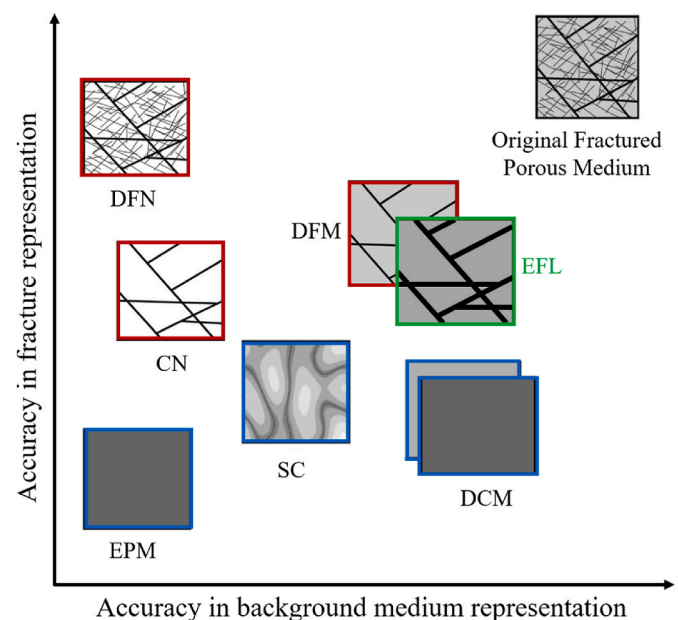


Fig. 1. Sketch comparing the accuracy of fractures and matrix modelling of different representation approaches. The suggested approach, EFL, (green frame) has the advantages of implicit approaches (blue) while generally yielding more accurate results like explicit approaches (red). Adapted from.<sup>46,48</sup> (For interpretation of the references to color in this figure legend, the reader is referred to the Web version of this article.)

fracture and matrix methods (DFM).<sup>49,50</sup> Such approaches, familiarly known as hybrid methods, can incorporate diverse implicit-explicit method combinations. Several complex models coupling DFM and multi-continuum approaches have been developed, e.g., a dual-permeability hybrid model combining DFM and the dual-permeability model.<sup>51</sup> While complex hybrid models have demonstrated the capability of producing accurate results, the issue of expensive computational resources remains. Therefore, simpler hybrid models are preferred whenever they are applicable. The simplest hybrid model known as the single-porosity hybrid model can be considered a simplified DFM model with reduced complexity. This model explicitly represents large fractures in a fractured medium and represents small-scale fractures and the matrix using a single continuum known as a pseudo-matrix.<sup>52</sup> To make this model a step simpler, the proposed method (EFL approach) can be used to represent explicit fractures as equivalent-continuum layers.

In this paper, we propose a new EFL approach to accurately model not only fluid flow, but also the geomechanical response in fractures with arbitrary orientation, represented as equivalent continua at a numerically tractable scale ( $\gg \mu\text{m}$ ). For illustrative purposes, we focus on a single fracture embedded in low-permeability rock matrix, resulting in distinctive flow time scales. The manuscript presents first the methodology for analytically calculating the equivalent hydromechanical properties of a fracture, represented as a layer with a thickness much larger than the actual aperture. Second, we verify the procedure by considering fluid injection into a fracture embedded in a low-permeability rock matrix by comparing results of a finite element model including the real aperture (reference model) with those of models including equivalent fracture layers. Next, we validate the approach by comparing numerical results against field data acquired during a hydraulic stimulation at the Bedretto Underground Laboratory for Geosciences and Geoenergies in Switzerland. Finally, we discuss the implications of our findings to introduce another simple, yet, practical fracture representation approach for fractured media.

## 2. Methodology

### 2.1. Governing equations

Transient fluid flow within a saturated fracture confined by a low-permeability rock matrix is governed by the flow equation<sup>53</sup>

$$\nabla \cdot (T \nabla h) = S \frac{\partial h}{\partial t} + r_s \quad (1)$$

where  $T$  [ $\text{L}^2\text{T}^{-1}$ ] is transmissivity,  $h = p/\gamma_w + z$  [L] is hydraulic head,  $p$  is fluid pressure [ $\text{ML}^{-1}\text{T}^{-2}$ ],  $\gamma_w$  [ $\text{ML}^{-2}\text{T}^{-2}$ ] is the specific weight of the fluid,  $z$  [L] is elevation from an arbitrary plane,  $S$  [–] is the storage coefficient,  $t$  [T] is time and  $r_s$  [ $\text{ML}^{-3}\text{T}^{-1}$ ] is a sink/source term, including from/to the matrix, which can be important during transient periods even for low permeability matrix (See Carrera and Martinez-Landa (2000) for details).<sup>54</sup> The mechanical process is solved by satisfying momentum balance that, neglecting inertial terms, reduces to the equilibrium of stresses

$$\nabla \cdot \boldsymbol{\sigma} + \mathbf{b} = \mathbf{0}, \quad (2)$$

where  $\boldsymbol{\sigma}$  [ $\text{ML}^{-1}\text{T}^{-2}$ ] is the total stress tensor and  $\mathbf{b}$  [ $\text{ML}^{-2}\text{T}^{-2}$ ] is the vector of body forces.

The relation between stress, strain, and pore pressure for isotropic materials within the linear elasticity theory for continuous media is given by Hooke's law

$$\Delta \boldsymbol{\sigma} = K \varepsilon_v \mathbf{I} + 2G \left( \boldsymbol{\varepsilon} - \frac{\varepsilon_v}{3} \mathbf{I} + \frac{\alpha}{2G} \Delta p \mathbf{I} \right), \quad (3)$$

where  $\varepsilon_v$  [–] is the volumetric strain,  $\boldsymbol{\varepsilon}$  [–] is the strain tensor,  $K = E/(3(1-2\nu))$  [ $\text{ML}^{-1}\text{T}^{-2}$ ] is the bulk modulus,  $G = E/(2(1+\nu))$

[ $\text{ML}^{-1}\text{T}^{-2}$ ] is the shear modulus,  $E$  [ $\text{ML}^{-1}\text{T}^{-2}$ ] is Young's modulus,  $\nu$  [–] is the Poisson ratio, and  $\alpha$  [–] is the Biot effective stress coefficient. In this work, we assume  $\alpha = 1$ , which leads to the strongest hydromechanical coupling.<sup>55</sup>

Equation (3) can be coupled with the flow equation through fluid pressure. Acknowledging that external loading and compressibility of the solid phase may affect water storage in the fracture, fluid mass conservation can be written as

$$\frac{\phi}{K_f} \frac{\partial p_f}{\partial t} + \frac{d}{dt} (\nabla \cdot \mathbf{u}) + \nabla \cdot \mathbf{q} = r_s, \quad (4)$$

where  $\phi$  [–] is porosity,  $K_f$  [ $\text{ML}^{-1}\text{T}^{-2}$ ] is the fluid bulk modulus,  $\mathbf{u}$  [L] is the displacement vector and  $\mathbf{q}$  [ $\text{L}^3\text{T}^{-1}$ ] is the fluid flux, given by Darcy's law. Note that Equations (3) and (4) can also be coupled through the volumetric strain, which can be expressed as the divergence of the displacement vector.

### 2.2. The embedded model

Consider an open fracture with hydraulic aperture  $b_f$  [L]. Fracture permeability is assumed to be isotropic and given by  $\mathbf{k} = k_f (\mathbf{I} - \mathbf{M})$  [ $\text{L}^2$ ], where  $\mathbf{I}$  [–] is the identity matrix,  $\mathbf{M}$  is the tensor of the fracture plane ( $M_{ij} = m_i m_j$ , where  $\mathbf{m}$  is the unit vector perpendicular to the fracture), and

$$k_f = \frac{b_f^2}{12}. \quad (5)$$

Equation (5) highlights the strong nonlinear relationship between fracture aperture and flow.<sup>1</sup> Acknowledging the strain dependence of intrinsic permeability is needed for coupled modeling in fractured media.<sup>56</sup> Variable fracture permeability can be computed by taking into account that aperture ( $\bar{b}_f$ ) is a function of volumetric strain<sup>57</sup>

$$\bar{b}_f = b_{0f} + (\varepsilon - \varepsilon_0) b_f \leq b_{maxf}, \quad (6)$$

$$k_f = k'_m + \frac{(b_{0f} + b_f \Delta \varepsilon)^2}{12}, \quad (7)$$

where  $k'_m$  [ $\text{L}^2$ ] is the intrinsic permeability of the matrix within the fracture layer,  $b_{0f}$  [L] and  $b_{maxf}$  [L] are the initial and maximum fracture aperture,  $\Delta \varepsilon$  [–] is the volumetric strain change ( $\Delta \varepsilon = \varepsilon - \varepsilon_0$ ), and  $\varepsilon_0$  [–] is a threshold strain.

### 2.3. Equivalent hydromechanical properties of a fracture

Three entities play roles in the equations governing HM problems: flux, storage, and displacement. These are controlled by transmissivity, storage coefficient, and stiffness, respectively. The adopted equivalent parameters of the equivalent fracture layer must represent the actual behavior of the real fracture (Fig. 2). In other words, both the actual fracture and the equivalent fracture layer should have the same transmissivity, storativity, and stiffness, both initially and along its time evolution.

The transmissivity of a fracture is given by the product of hydraulic conductivity and aperture

$$T_f = \frac{\rho g}{\mu} k_f b_f = \frac{\rho g}{\mu} \frac{b_f^3}{12}, \quad (8)$$

where  $\rho$  [ $\text{ML}^{-3}$ ] is fluid density,  $g$  [ $\text{LT}^{-2}$ ] is gravity, and  $\mu$  [ $\text{ML}^{-1}\text{T}^{-1}$ ] is fluid viscosity. The dependence of transmissivity on  $b_f^3$  is the essence of the well-known cubic law<sup>7</sup> and expresses that fracture transmissivity is extremely sensitive to small changes in aperture. The Equivalent fracture layer with thickness of  $b_{eq}$  should carry the same flow rate as the actual fracture:

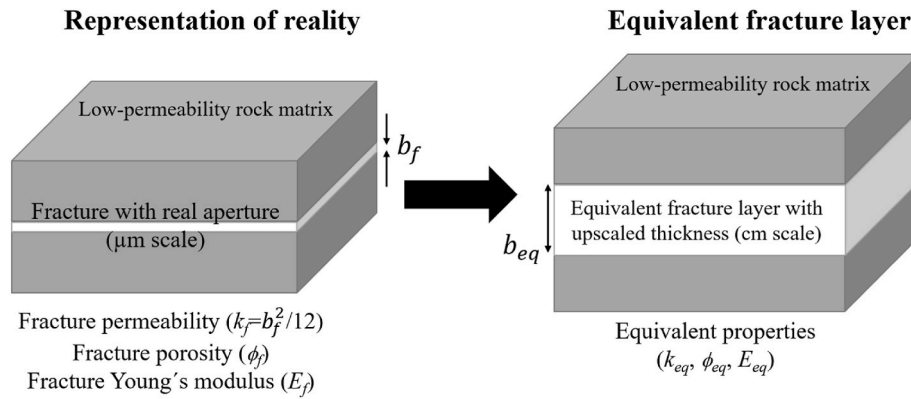


Fig. 2. Concept of the equivalent fracture layer representing a real fracture.

$$T_{eq} = T_f \rightarrow k_{eq} b_{eq} = k_f b_f. \quad (9)$$

where  $k_{eq}$  [ $L^2$ ] is the intrinsic permeability of the equivalent fracture layer. When equating the actual and equivalent fracture properties to represent the actual fracture aperture ( $b_f$ ) by an equivalent continuum layer with a thickness  $b_{eq}$ , the equivalent hydromechanical fracture transmissivity, stiffness, and storativity become a function of the equivalency coefficient

$$\xi = \frac{b_f}{b_{eq}}. \quad (10)$$

To have the same transmissivity, equivalent parameters can be derived from equations (7) and (9) as

$$k'_{meq} = \xi k'_{mf}, b_{0eq} = b_{of}, b_{max,eq} = b_{max,f}, \epsilon_{eq} = \xi \epsilon_f, \quad (11)$$

where the subscript  $f$  and  $eq$  denote the properties of the fracture with its actual aperture and equivalent fracture layer, respectively.

The mechanical behavior of fractures can be characterized by normal and shear stiffnesses<sup>58,59</sup>

$$\sigma_n = \lambda_n u_n, \tau_s = \lambda_s u_s \quad (12)$$

where  $\sigma_n$  [ $ML^{-1}T^{-2}$ ] and  $\tau_s$  [ $ML^{-1}T^{-2}$ ] are normal and shear stresses,  $\lambda$  [ $ML^{-2}T^{-2}$ ] is stiffness, and  $u$  [ $L$ ] is displacement. The superscripts  $n$  and  $s$  denote normal and shear components, respectively. In general, one may expect  $\lambda_s$  to be itself a tensor, especially if the fracture is shear origin. In such case, irregularities tend to align with shear direction (orthogonal to the open channels), so that  $\lambda_s$  will be initially smaller in this direction. For the sake of simplicity and assuming that the impact of the initial irregularities diminishes as the fracture opens, we will assume scalar  $\lambda_s$ . Normal and shear stiffnesses of an arbitrary-oriented fracture can be obtained as<sup>58,59</sup>

$$\lambda_n = \frac{E_{of}}{b_f}, \lambda_s = \frac{G}{b_f}, \quad (13)$$

where  $E_{of}$  is an apparent oedometric modulus of the fracture. If the deformation out of the fracture plane is constrained, the modulus  $E_o$  is defined as

$$E_{of} = \frac{1 - \nu}{(1 + \nu)(1 - 2\nu)} E_f. \quad (14)$$

From equations (13) and (14), fracture stiffnesses can be determined as

$$\lambda_n = \frac{1 - \nu}{(1 + \nu)(1 - 2\nu)} \frac{E_f}{b_f}, \lambda_s = \frac{E_f}{2b_f(1 + \nu)}. \quad (15)$$

where  $E_f$  and  $\nu$  are the apparent Young's modulus and Poisson ratio of

the fracture. Maintaining normal and shear stiffnesses and knowing that  $\lambda_s = \lambda_n \frac{(1-2\nu)}{2(1-\nu)}$  from elasticity, the equivalent Young's modulus and Poisson's ratio of the equivalent fracture layer can be obtained by

$$E_{eq} = \frac{3\lambda_n - 4\lambda_s}{\lambda_n - \lambda_s} \lambda_s b_{eq}, \nu_{eq} = \frac{\lambda_n - 2\lambda_s}{2(\lambda_n - \lambda_s)}, \text{ with } \lambda_n > 2\lambda_s. \quad (16)$$

In principle, the aperture and stiffness of the real fracture can be estimated (or measured) and, from them, the equivalent properties of the equivalent fracture layer can be easily calculated. This formulation applies to both fractures with and without infilling.

Finally, both layers should have same storativity as

$$S_{eq} = S_f \rightarrow S_{seq} b_{eq} = S_f b_f, \quad (17)$$

where  $S_s$  [ $L^{-1}$ ] is the specific storage (i.e.,  $\rho g(\phi\beta_w + \beta_x)$ ),  $\beta_w$  [ $M^{-1}LT^2$ ] is the compressibility of the fluid, and  $\beta_x = 3(1-2\nu_x)/E_x$  [ $M^{-1}LT^2$ ] is the bulk compressibility of the layer  $x$  (either fracture ( $\beta_f$ ) or equivalent layer ( $\beta_{eq}$ )). Expanding the equation, we can calculate equivalent porosity as

$$\phi_{eq} = \xi \phi_f. \quad (18)$$

### 3. Model verification and validation

#### 3.1. A single fracture embedded in a low-permeability matrix

##### 3.1.1. Model setup

We numerically model a single circular fracture in which water is injected into its center through a well with radius  $r_w = 0.1$  m (Fig. 3). As reference, we model the fracture with actual properties and compare results to models with an equivalent fracture layer. The axisymmetric model represents a 100-m radius horizontal circular fracture with uniform thickness (10  $\mu$ m as real aperture) embedded between two 10-m thick layers of low-permeability rock at a depth of 1 km. The large radial extent of the fracture is such that the nature of the outer boundary, i.e., prescribed hydrostatic pressure or no flow, does not affect results during the injection. Both fracture and rock matrix continua have homogeneous and isotropic properties. Boundary conditions include zero horizontal displacement at both inner and outer lateral boundaries and zero vertical displacement at the bottom boundary. A constant flow rate  $q = 50$  kg/s/m<sup>2</sup> is injected at the fracture segment of the inner boundary. A constant initial stress field ( $\sigma_x = 15$  MPa,  $\sigma_y = 25$  MPa,  $\sigma_z = 15$  MPa) and a linear hydrostatic pressure gradient (10 and 10.2 MPa at model top and bottom, respectively) are applied to the model. The fracture is assumed to be clean, i.e., actual porosity is set to 1, and its initial intrinsic permeability is calculated using Equation (5), which results in  $k_f = 8.33 \cdot 10^{-12}$  m<sup>2</sup>. Input parameters for the matrix, fracture, and equivalent fracture layers are listed in Fig. 3 and Table 1.

We build three additional models with increasing thickness of the

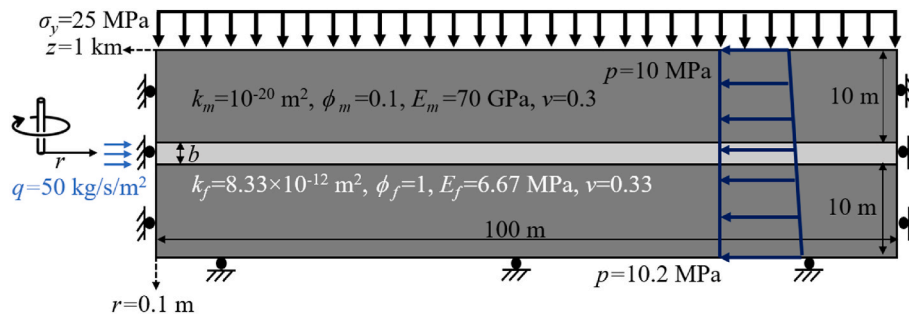


Fig. 3. Sketch of the axisymmetric model used for verification purposes: geometry, boundary, and initial conditions. Input parameters are indicated in the insets, where subscripts m and f denote matrix and fracture respectively (see also Table 1).

Table 1

Input parameters for the fracture and equivalent fracture layer models used for verification purposes.

Fracture aperture (m)	$\xi = \frac{b_f}{b_{eq}}$	Fracture Permeability (m <sup>2</sup> )	Porosity (-)	Injection flux (kg/s)	Young's modulus (MPa)
Original fracture	1	8.33·10 <sup>-12</sup>	1	50	6.67
Equivalent fracture layer models					
0.001	10 <sup>-2</sup>	8.33·10 <sup>-14</sup>	10 <sup>-2</sup>	0.5	667
0.01	10 <sup>-3</sup>	8.33·10 <sup>-15</sup>	10 <sup>-3</sup>	0.05	6670
0.1	10 <sup>-4</sup>	8.33·10 <sup>-16</sup>	10 <sup>-4</sup>	0.005	66700

equivalent fracture layer and apply the equivalent properties, i.e., permeability, porosity, and Young's modulus (Poisson's ratio is independent of the equivalent layer thickness) using the relationships derived in Section 2.3. A common structured finite element mesh consisting of 12,322 quadrilateral elements is used as spatial discretization for all models. The fracture consists of 5 rows of elements, whereas the matrix slabs contain 30 rows of elements in the vertical direction. The elements in the matrix are concentrated toward the fracture-matrix interfaces to capture the leak-off more accurately. Also, for the sake of accuracy, finite elements are concentrated towards the well to properly capture fluxes caused by injection and corresponding pressure variations in both fracture and matrix. We have performed a mesh sensitivity analysis to ensure that further refinement does not affect the results, not displayed here for the sake of brevity. The models simulate water injection at a constant rate for 30 h and are run twice, considering both constant and variable fracture permeability depending on deformation. We analyze the pressure evolution at the injection well ( $r_w = 0.1$  m) and the hydromechanical response along the fracture at the end of the

injection. The fully coupled hydromechanical numerical models are implemented using the finite element software CODE\_BRIGHT.<sup>60,61</sup>

The injected volumetric flow rate into a fracture,  $Q$  [L<sup>3</sup>T<sup>-1</sup>], must be conserved when representing fracture thickness with the equivalent fracture layer approach. Given that the flux injected into a layer through a fully penetrating well equals  $q = Q/A$ , where  $A$  [L<sup>2</sup>] is the cross-sectional area to flow, i.e.,  $2\pi r_w w$ ,  $r_w$  [L] being the radius of the well and  $w$  [L] the thickness through which fluid is injected, the equivalent injection flux into the equivalent fracture layer, is  $q_{eq} = \xi q_f$  where  $q_f = Q/(2\pi r_w b_f)$  is the injection flux for the actual fracture.

### 3.1.2. Numerical results

Both the pore pressure evolution at the injection well and the radial pressure distribution are reproduced accurately by the models with equivalent fracture layers compared to the reference model with explicit fracture representation (Fig. 4). The pressure evolution curves (in Fig. 4a) follow the typical Hantush leaky solution.<sup>62</sup> At the beginning of injection, after a short transition, it follows Theis solution<sup>63</sup> as storage in and leakage into the matrix are neglected, then, during a transition period, leak-off starts to play a role and decreases the pressure build-up. For the time scale of our analysis, i.e., 30 h, the low-permeability of the rock matrix does not allow the pressure evolution curve to reach to the fracture-matrix Theis solution (where both fracture and matrix act as a single system with steady state leakage and combined storage). Considering variable permeability decreases pressure build-up due to permeability enhancement since early times (less than a second), when volumetric strain starts to accumulate (Fig. 4a, blue curves). Constant injection in the fracture forms a conical pressure profile versus radial distance (Fig. 4b).

Pressure build-up in the variable permeability model with  $b_{eq} = 10$  cm (blue dotted line in Fig. 4a) starts to slightly deviate from the

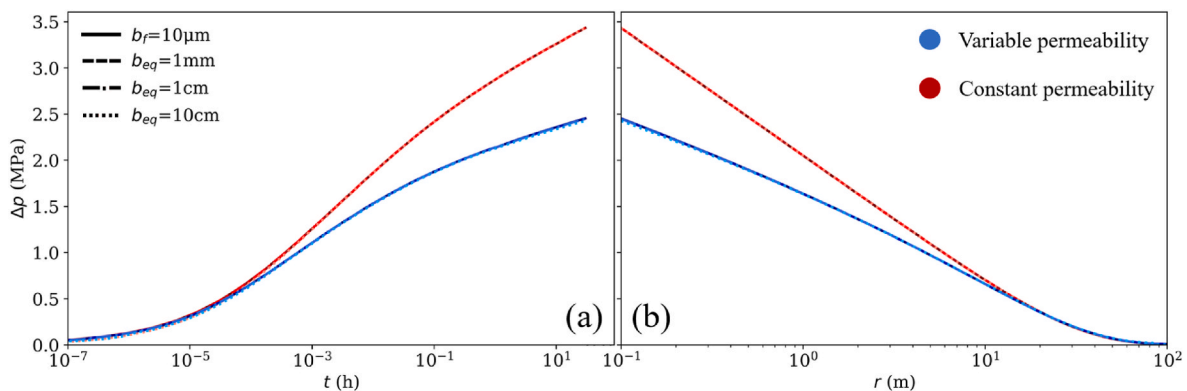


Fig. 4. a) Pressure evolution at the injection well for reference models (actual fracture aperture; solid lines) and models with equivalent fracture layer for both constant (red lines) and variable (blue lines) permeability during constant flow injection; line styles correspond to different fracture apertures. b) Radial pressure profile along the horizontal mid-line of the fracture at the end of the injection (30 h). Note that the curves overlap, indicating that the proposed methodology is accurate. (For interpretation of the references to color in this figure legend, the reader is referred to the Web version of this article.)

reference curve after ca. 2 h of injection. This deviation is caused by more permeability enhancement ratio in that model compared to other models, which means transmissivity is no longer maintained constant for the equivalent model (Fig. 5). In other words, the smaller is the equivalent aperture, the closer the model reproduces the reference case, as expected. This deviation could limit the upper bound of the equivalent aperture for an equivalent fracture layer since the coupled hydro-mechanical response not any more reflect the reference solution. However, models with 1 cm and 1 mm equivalent apertures yield well fitted results.

The embedded model employed here to account for variable permeability is a function of volumetric strain and discrepancy in models with larger equivalent aperture (i.e., 10 cm) stems from a different mechanical response of the fracture. Fig. 6 shows stress profiles along the horizontal mid-line of the fracture, where lower compressive stresses are mobilized around the injection well at the end of the injection (30 h) for the thickest equivalent fracture layer. The poromechanical stress increase in the longitudinal direction along the fracture (Fig. 6a) is significantly larger than in the direction perpendicular to it (Fig. 6b), which has implications for fracture stability.<sup>64</sup> It is worth mentioning that the differences between the mechanical responses of the  $b_{eq} = 10$  cm models against the reference model are smaller in the variable permeability model because of the lower pressure build-up compared to the constant permeability models (Fig. 4a).

Lower pressure build-up leads to smaller fracture opening in variable permeability models. Fracture layer apertures open around 3.0 and 2.2  $\mu\text{m}$  for constant and variable permeability models, respectively (Fig. 7; opening is calculated based on displacement difference of top and bottom of the fracture). Although  $b_{eq} = 10$  cm model reproduces the pressure evolution better in the constant permeability model in comparison to the variable permeability model (Fig. 4a), it is less accurate in reproducing aperture enhancement in the constant permeability model. Note that the variable permeability models represent the actual fracture behavior more realistically than constant permeability models because fractures open in response to injection-induced overpressure, yielding significant permeability enhancement as a result of the cubic law (equation (5)).

Vertical displacement at the top of the overlying rock layer in response to fluid injection presents a constant value until a radius of around 3 m and it follows a typical bell shape further away (Fig. 8). The displacement in variable permeability models is lower due to the smaller pressure build-up (Fig. 4b). The discrepancy of the  $b_{eq} = 10$  cm model compared with the reference solution is around 14 % and it is related to differences in the fracture aperture changes (Fig. 7).

### 3.2. Bedretto experiment

#### 3.2.1. Model setup

We validate our fracture representation approach with an equivalent fracture layer by comparing numerical results with field data acquired during the hydraulic stimulation of a fracture at the Bedretto Underground Laboratory for Geosciences and Geoenergies (BULGG; see more detailed information in [www.bedrettolab.ethz.ch](http://www.bedrettolab.ethz.ch)). BULGG enables medium-to large-scale in-situ experiments with a focus on hydraulic stimulation and fault reactivation (Fig. 9). The overburden directly above the laboratory is approximately 1500 m, providing conditions that start to resemble realistic EGS systems (scale 1:3 approximately).<sup>10,65</sup> To characterize the rock mass, several boreholes were drilled perpendicular to the tunnel axis with lengths ranging from 100 m to 400 m MD (Measured Depth; Fig. 9c). A large number of hydraulic stimulation tests have been and are being performed at BULGG to stimulate the intersected fractures.<sup>65</sup> Based on stress measurements,<sup>66</sup> BULGG is in a normal faulting and/or strike-slip stress regime, and the rock mass is close to be critically stressed.<sup>67,68</sup>

We develop a 2D plane-strain numerical model to simulate the hydraulic stimulation in Bedretto. It comprises an inclined plane dipping (on average)  $42^\circ$  downwards following the trajectory of the boreholes and has a large extension covering around  $75 \text{ km}^2$  of the site (Fig. 10a). The Bedretto gallery is located at the center of the upper boundary of the model (Fig. 10b) and the bottom boundary is at a true vertical depth of 5000 m ( $-7472.4$  m in the inclined model). The model comprises the main characterization boreholes (MB1 to MB4) and the two main stimulation boreholes (ST1 and ST2) as well as the major fracture and shear zones identified through borehole logging and geological structural analysis.<sup>10,69</sup> In the fracture intersections, we assign the properties of the more permeable fracture to the intersection. We use an unstructured mesh that consists of 27,248 quadrilateral elements and 27,420 nodes and is highly refined at the closest vicinity of the modeled fracture/shear zones and the boreholes. Both sides and the bottom of the model are fixed against lateral and vertical displacements, respectively. A linear distributed fluid pressure and initial stresses are applied to the model from top to bottom (Fig. 10a).

Fractures are modeled as an elastic continuum medium with homogeneous hydromechanical properties. We use the embedded model to compute fracture permeability changes according to equation (7). As a result, fracture permeability varies with distance from the injection well, being largest near the well and approaching the initial value further away from the pressurization front, where the fracture has not undergone overpressure-induced opening. Table 2 lists the equivalent parameters of the stimulated fracture and rock matrix properties used in the numerical simulation. The properties of the rock matrix are derived

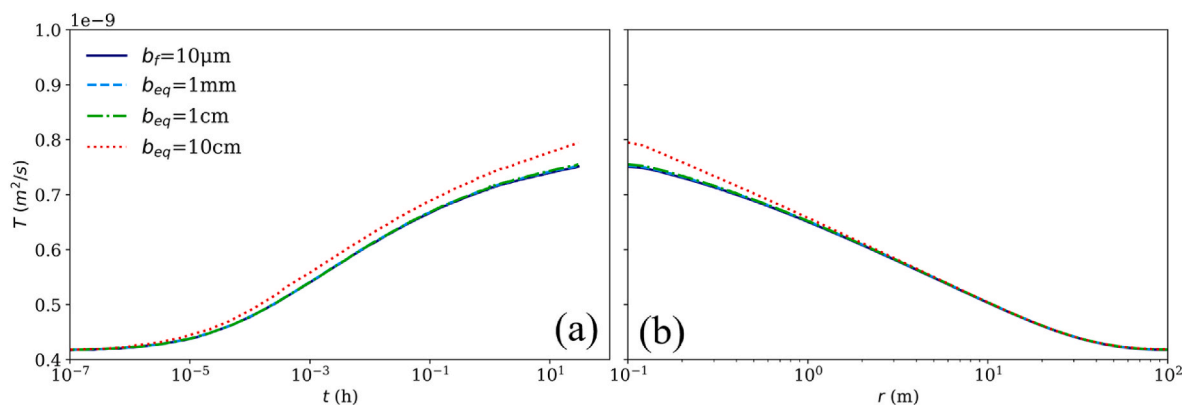


Fig. 5. Transmissivity enhancement (a) and profile along the horizontal mid-line of the fracture at the end of the injection (30 h) (b) caused by accumulated deformation in the reference model (solid lines) and models with equivalent fracture layers (variable permeability cases). The magnitude orders of permeability are defined during fracture representation, yet, the enhancement rates are similar in all models except  $b_{eq} = 10$  cm model which shows more enhancement.

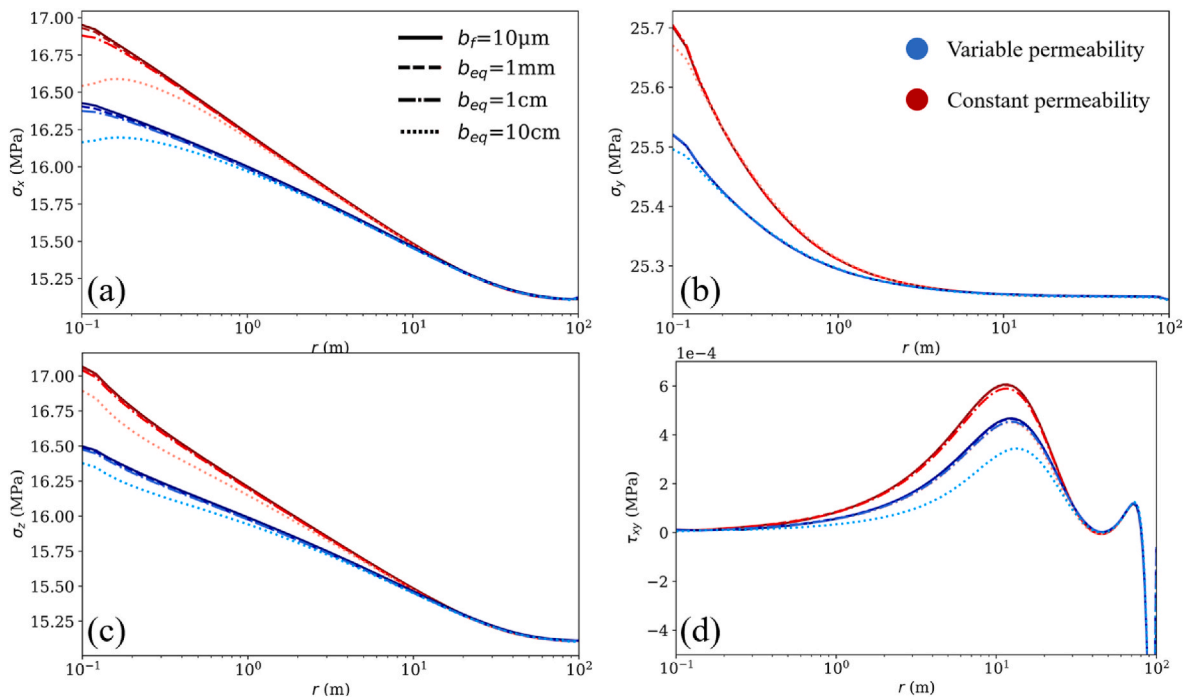


Fig. 6. Profiles of stress components along the horizontal mid-line of the actual fracture and equivalent layers for both constant (red) and variable (blue) permeability models. (For interpretation of the references to color in this figure legend, the reader is referred to the Web version of this article.)

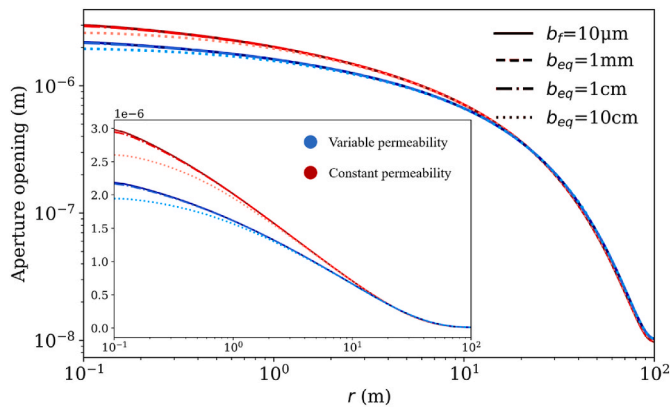


Fig. 7. Fracture aperture change along the horizontal mid-line of the actual fracture (solid) for both constant (red) and variable (blue) permeability equivalent models in log-log and semi-log scales at the end of the injection (30 h). Aperture changes are calculated by displacement difference between top and bottom of the fractures. (For interpretation of the references to color in this figure legend, the reader is referred to the Web version of this article.)

from field measurements, whereas the properties of the equivalent fracture layer are the equivalent parameters based on the field measurements of the real fracture. The modeling sequence includes the tunnel drainage effect on pore pressure during and after excavation and the subsequent consolidation covering 40 years (since the end of the tunnel excavation). The injection interval is within borehole MB1 (Fig. 10c), in which water is injected through an isolated section into the fracture at a measured depth of 267 m (true vertical depth 188.8 m).

### 3.2.2. Simulation of the field injection test

The numerical simulation covers the first 40 min of the field experiment, which overall lasted 8 h, because this is the period during which the fracture behaves elastically, i.e., subsequently, the fracture deforms irreversibly (see Vaezi et al. 2024 for more details).<sup>71</sup> Fig. 11 compares

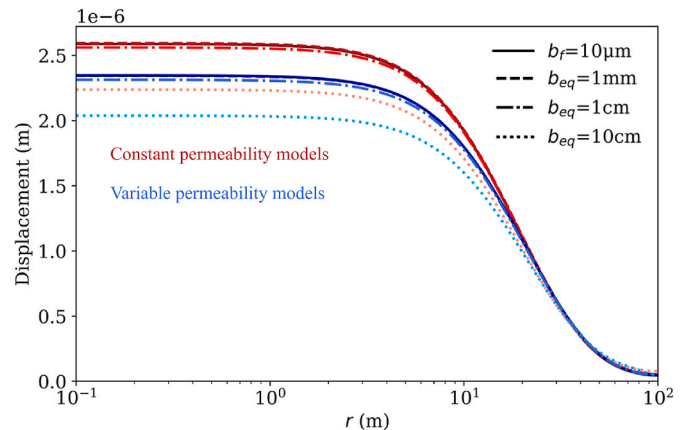


Fig. 8. Vertical displacement at the top boundary of the model versus radial distance at the end of the injection (30 h).

the temporal evolution of the generated overpressure at the injection interval predicted by the numerical model against the experimental data. The model accurately reproduces field measurements, with a small discrepancy at the beginning of each injection steps, which we attribute to non-modeled equipment compliance effects. Despite these small deviations, (1) simulated and measured trends are very similar, and (2) simulated injection pressure fits well the field data from the mid-times of each injection step.

The embedded model used in this simulation enhances permeability of the fracture in the vicinity of the injection interval (around 6 m) after 40 min of injection (Fig. 12). Note that, in our model, the behavior of the fracture is assumed to be elastic and the permeability enhancement in the embedded model is based on elastic strains only. After 40 min of injection, the fracture shears and activates, which leads to plastic deformations and irreversible permeability gain.<sup>71</sup> Permeability linearly increased around 7% at a point near the injection interval after 40 min of injection which was not enough to reach the jacking pressure. Notably

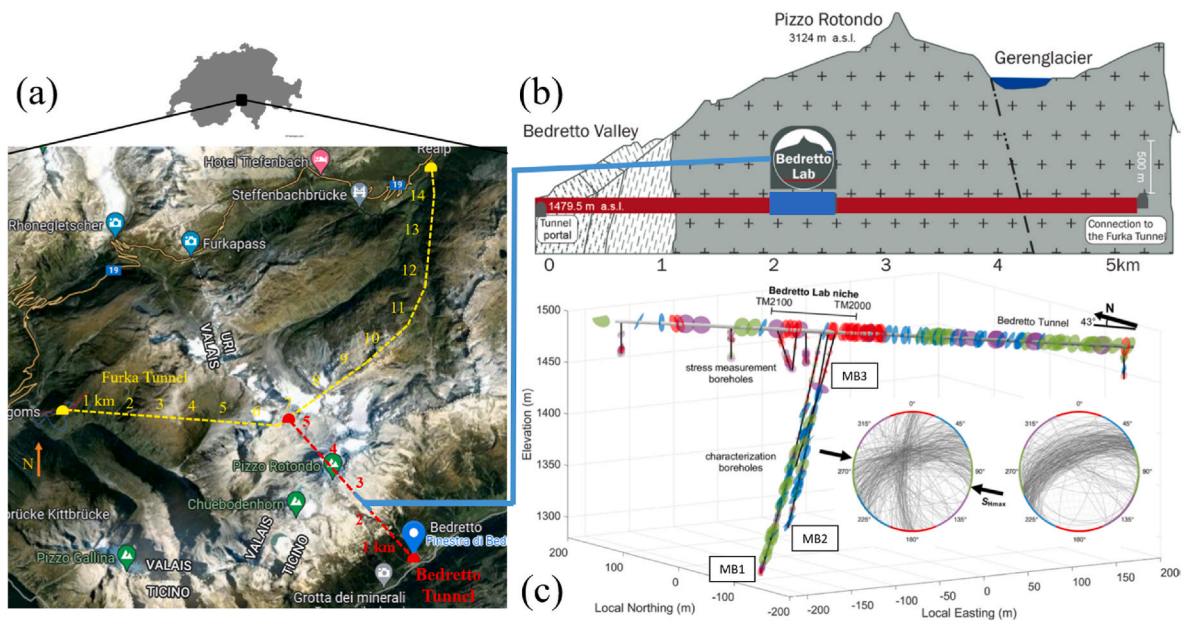


Fig. 9. a) Location and trace of the Bedretto gallery excavated in Rotondo granite in Switzerland. b) Cross-sectional view of the Bedretto lab through the tunnel.<sup>69,70</sup> c) Configuration of the MB1, MB2 and MB3 boreholes with respect to the Bedretto Tunnel. Fractures and fault zones, mapped along the tunnel and intersected by the boreholes, are colored according to fracture strike.<sup>69</sup>

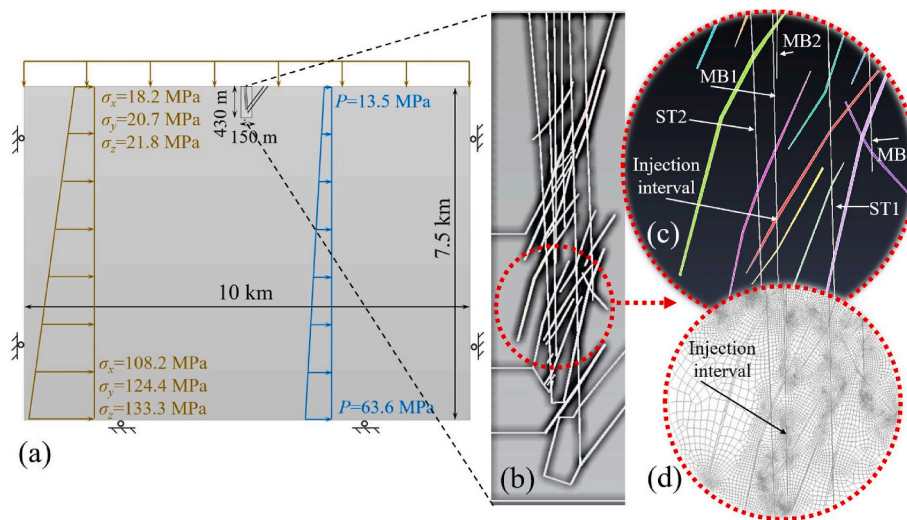


Fig. 10. a) Model geometry, boundary and initial conditions, and state of stress at top and bottom boundaries. b) Configuration of wellbores and the identified fracture/shear zones within the model. c) Detailed view around the stimulated fracture (in red). d) Mesh configuration of the same detailed view. (For interpretation of the references to color in this figure legend, the reader is referred to the Web version of this article.)

Table 2  
Input parameters for rock matrix and equivalent fracture layer.

	$E$ (GPa)	$\nu$	$\phi$	$k$ (m <sup>2</sup> )			
				$k_m$ (m <sup>2</sup> )	$b_0$ (m)	$a$ (m)	$b_{max}$ (m)
Fracture (equivalent)	23	0.37	0.005	$5 \times 10^{-17}$	2.25	0.01	$1.34 \times 10^{-4}$
Rock matrix	46	0.37	0.005	$2.5 \times 10^{-18}$			

in the vicinity of ST2 well the permeability of the fracture has a spike governed by the permeability of the well.

#### 4. Discussions

Numerical modeling of fractured media faces the grand challenge of representing fractures and matrix with spatial scales and flow characteristic times that differ orders of magnitude. In a kilometer-scale reservoir problem, it is difficult to express the micrometer aperture of actual fractures using a 1:1-scale element. We demonstrate that a viable approach is the Equivalent Fracture Layer (EFL), which represents fractures with an equivalent continuum while maintaining fracture transmissivity, storage coefficient and stiffness to preserve flow, stress, and deformation. By incorporating fracture-matrix interaction, EFL enables the representation of leak-off from fractures into the surrounding

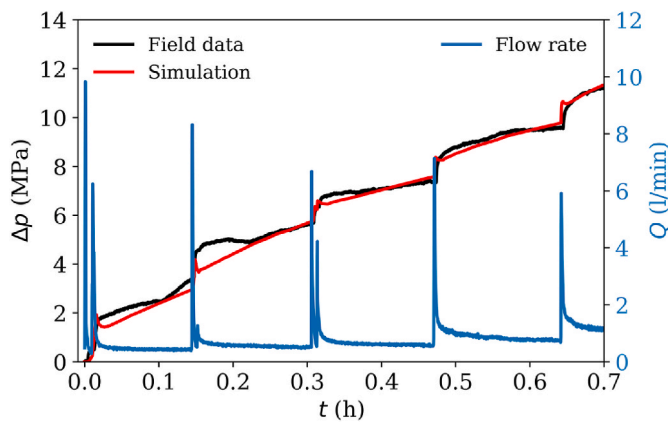


Fig. 11. Pressure evolution at the injection interval reproduced by the numerical model (red line) against injection pressure measured at the field (black line) as well as fluid injection rate (blue line). (For interpretation of the references to color in this figure legend, the reader is referred to the Web version of this article.)

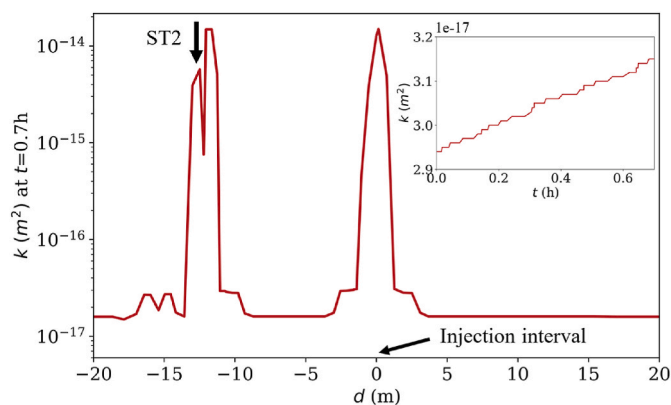


Fig. 12. Permeability profile in the middle of the fracture ( $d$  is the distance along the middle of the fracture) at the end of the injection period ( $t = 0.7$  h) in both sides of the injection interval (located at  $d = 0$ ); In the inset: permeability evolution at a point near the injection interval.

rock matrix, even in very low-permeability rock formations.<sup>71</sup> The EFL approach offers advantages comparable to continuum methodologies, including reduced computational cost and a commensurate level of accuracy compared to explicit techniques.<sup>43</sup> The equivalent properties through an adequate fracture representation (Section 2.3) provide an approach to employ a layer with a thickness several orders of magnitude larger than the actual fracture aperture, thus alleviating discretization issues whilst reproducing the behavior of the actual fracture with accuracy even within field-scale models that include multiple fractures.<sup>71–73</sup> The method can be used both in 2D and 3D models, implying the latter a significantly larger computational cost. The EFL method has been used to estimate fracture stability changes and assess induced seismicity.<sup>64,71–76</sup>

Simulation results show that there is an upper bound for the validity of the suggested representation approach. Although the model with  $b_{eq} = 10$  cm yields accurate results for the hydraulic analysis (Fig. 4), the hydromechanical response is not as accurate as models with thinner apertures (Figs. 5–7). It is worth mentioning that we have noticed that when  $E_{eq}$  exceeds Young's modulus of rock matrix ( $E_m$ ), the results become unreliable. For instance, the equivalent modulus is  $E_{eq} = 66$  GPa (for  $b_{eq} = 10$  cm model) and we had to set  $E_m = 70$  GPa to have a reliable result. This is another limiting upper bound factor for the proposed approach. However, using  $b_{eq} = 1$  cm provides the required accuracy as

well as a convenient discretization process.

Suffice to say that the closer is the equivalent aperture to the actual one, the better is the accuracy as expected, especially in the mechanical response. However, differentiating between  $b_{eq} = 1$  cm and  $b_{eq} = 1$  mm models is difficult and the results are almost the same. This reinforces the applicability of the methodology, since we get what we expected. Furthermore, the method can be applied to any geometry of the fracture and with multiple fractures, as we have applied to a complex fracture network like the Bedretto experiment. Our approach is based on cubic law derived under the setting of smooth parallel plates and we have assigned larger permeability and weaker properties in the fracture intersections. Yet, fracture intersections can be much more permeable than what results from a simple superposition of the cubic law. For example, some fracture intersections may exhibit a local network of spider-web like fractures connecting the two intersecting fractures and fluid flow converges and deflects at the intersections.<sup>77,78</sup> Thus, further improvements may be required in how to handle fractures intersection.

EFL method exhibit an advantageous capability of effectively capturing the distinct effects of fractures like discrete methods such as DFN and DFM methods. However, DFN method suffers when dealing with the leaky nature of fractures in fluid injections and temporal scales that require consideration of matrix diffusion.<sup>79</sup> Preferably, fully-explicit fracture network representation employing DFM methods would circumvent any error arising from upscaling procedures in EPM methods.<sup>80</sup> However, limitations on computational resources entail the use of continuum methods in conjunction with DFM methods. Explicit integration of fractures within numerical models may be imperative under specific scenarios to ensure the fidelity of coupled multiphysics simulations, where the EFL method offers a computationally efficient alternative to DFM approaches.<sup>43</sup> For instance, including fractures in models may be necessary in cases where induced seismicity might be an issue and should be forecasted accurately.<sup>81</sup> The use of the EFL approach has revealed that despite the EPM approach, the EFL methods are able to reproduce a very similar pressure evolution at the injection and production wells, substantial disparities arise in the pore pressure distribution within the fractured rock when neglecting fractures by homogenizing the fractured media by an equivalent one.<sup>36</sup>

For a porous medium in which the properties of fracture networks vary between zones, different models might be employed in each zone to diminish the total required computational expenses. Our proposed EFL approach validated by reproducing the field experiment result at Bedretto presents a simple, yet, effective method to utilize in the modeling and to understand coupled processes in fractured media related to geo-resources applications.

## 5. Conclusions

We have derived equivalent hydromechanical properties for an equivalent-continuum layer that is several orders of magnitude thicker than the represented fracture. We have obtained identical simulation results for equivalent fracture layers represented with cm-scale thickness as the actual fracture aperture (which is in the  $\mu\text{m}$  scale). Employing this method, the discretization of fractures is much more tractable while the accuracy is maintained. Much remains to be done such as applying the method to complex fracture networks, still, we have validated the fracture representation approach by reproducing a field experiment of water injection into a fracture at Bedretto. Thus, the equivalent fracture layer approach represents a useful method to model geo-energy and geo-engineering applications in fractured media involving scales differing several orders of magnitude to handle discretization problem.

## Open research

The extensively validated fully-coupled finite element code, CODE\_BRIGHT, can be accessed freely at the developer page: [https://deca.upc.edu/en/projects/code\\_bright](https://deca.upc.edu/en/projects/code_bright).

Data can be accessed at: <https://digital.csic.es/handle/10261/339672>.

### CRedit authorship contribution statement

**Iman Vaezi:** Writing – review & editing, Writing – original draft, Visualization, Validation, Software, Methodology, Investigation, Formal analysis, Data curation. **Francesco Parisio:** Supervision, Formal analysis, Conceptualization. **Keita Yoshioka:** Writing – review & editing, Formal analysis. **Andres Alcolea:** Writing – review & editing, Software, Resources, Investigation, Formal analysis. **Peter Meier:** Resources. **Jesús Carrera:** Writing – review & editing, Formal analysis. **Sebastià Olivella:** Writing – review & editing, Formal analysis. **Victor Vilarrasa:** Writing – review & editing, Supervision, Software, Project administration, Methodology, Investigation, Funding acquisition, Formal analysis, Conceptualization.

### Declaration of competing interest

The authors declare that they have no known competing financial interests or personal relationships that could have appeared to influence the work reported in this paper.

### Data availability

Data can be accessed at: <https://doi.org/10.20350/digitalCSIC/15692>.

### Acknowledgments

I.V. and V.V. acknowledge funding from the European Research Council (ERC) under the European Union's Horizon 2020 Research and Innovation Program through the Starting Grant GEOREST ([www.georest.eu](http://www.georest.eu)), under grant agreement No. 801809. J.C. and V.V. acknowledge financial support from the "ZoDrEx" project, which has been subsidized through the ERANET Cofund GEOTHERMICA (Project no. 731117), from the European Commission and the Spanish Ministry of Economy, Industry and Competitiveness (MINECO). The work of Geo-Energie Suisse AG was financially supported by the Swiss Federal Office of Energy within the framework of the ZoDrEx GEOTHERMICA project under contract SI/501720-01. F. P. acknowledges funding from the European Union's Horizon 2020 Research and Innovation Program through the Marie Skłodowska-Curie Individual Fellowship ARMI-STICE, Spain under Grant Agreement No. 882733. K.Y. acknowledges funding from EURAD, the European Joint Programme on Radioactive Waste Management through the project DONUT (Grant No 847593). IMEDEA is an accredited "Maria de Maeztu Excellence Unit" (Grant CEX2021-001198, funded by MCIN/AEI/10.13039/501100011033). IDAEA-CSIC is a Center of Excellence Severo Ochoa (Spanish Ministry of Science and Innovation, Project CEX2018-000794-S).

### References

- Adler PM, Thovert JF, Mourzenko VV. *Fractured Porous Media*. OUP Oxford; 2013.
- Parisio F, Yoshioka K. Modeling fluid reinjection into an enhanced geothermal system. *Geophys Res Lett*. 2020;47(19), e2020GL089886. <https://doi.org/10.1029/2020GL089886>.
- Xu H, Rutqvist J, Birkholzer J. A study of thermal pressurization and potential for hydro-fracturing associated with nuclear waste disposal in argillaceous claystone. *Int J Rock Mech Min Sci*. 2020;136, 104536. <https://doi.org/10.1016/j.ijrmm.2020.104536>.
- Vilarrasa V, Olivella S, Carrera J, Rutqvist J. Long term impacts of cold CO<sub>2</sub> injection on the caprock integrity. *Int J Greenh Gas Control*. 2014;24:1–13. <https://doi.org/10.1016/j.ijggc.2014.02.016>.
- Vilarrasa V, Carrera J, Olivella S. Hydromechanical characterization of CO<sub>2</sub> injection sites. *Int J Greenh Gas Control*. 2013;19:665–677. <https://doi.org/10.1016/j.ijggc.2012.11.014>.
- Tsang YW. Usage of "Equivalent apertures" for rock fractures as derived from hydraulic and tracer tests. *Water Resour Res*. 1992;28(5):1451–1455. <https://doi.org/10.1029/92WR00361>.
- Witherspoon PA, Wang JSY, Iwai K, Gale JE. Validity of Cubic Law for fluid flow in a deformable rock fracture. *Water Resour Res*. 1980;16(6):1016–1024. <https://doi.org/10.1029/WR016i006p01016>.
- Guimerà J, Carrera J. A comparison of hydraulic and transport parameters measured in low-permeability fractured media. *J Contam Hydrol*. 2000;41(3):261–281. [https://doi.org/10.1016/S0169-7722\(99\)00080-7](https://doi.org/10.1016/S0169-7722(99)00080-7).
- De Simone S, Vilarrasa V, Carrera J, Alcolea A, Meier P. Thermal coupling may control mechanical stability of geothermal reservoirs during cold water injection. *Phys Chem Earth, Parts A/B/C*. 2013;64:117–126. <https://doi.org/10.1016/j.pce.2013.01.001>.
- Meier P, Guinot F, Bethmann F, et al. ZoDrEx an European endeavour for optimising zonal isolation, drilling and exploitation of EGS projects. In: *Proceedings World Geothermal Congress*. 2020:1.
- Flemisch B, Berre I, Boon W, et al. Benchmarks for single-phase flow in fractured porous media. *Adv Water Resour*. 2018;111:239–258. <https://doi.org/10.1016/j.advwatres.2017.10.036>.
- Alcolea A, Kuhlmann U, Marschall P, et al. A pragmatic approach to abstract the EDZ around tunnels of a geological radioactive waste repository—application to the HG-A experiment in Mont Terri. *Geological Society, London, Special Publications*. 2016;443(8). <https://doi.org/10.1144/SP443>.
- Martinez-Landa L, Carrera J. A methodology to interpret cross-hole tests in a granite block. *J Hydrol*. 2006;325(1):222–240. <https://doi.org/10.1016/j.jhydrol.2005.10.017>.
- Hyman JD, Gable CW, Painter SL, Makedonska N. Conforming delaunay triangulation of stochastically generated three dimensional discrete fracture networks: a feature rejection algorithm for meshing strategy. *SIAM J Sci Comput*. 2014;36(4):A1871–A1894. <https://doi.org/10.1137/130942541>.
- Fumagalli A, Keilegavlen E, Scialo S. Conforming, non-conforming and non-matching discretization couplings in discrete fracture network simulations. *J Comput Phys*. 2019;376:694–712. <https://doi.org/10.1016/j.jcp.2018.09.048>.
- Lei Q, Latham JP, Tsang CF. The use of discrete fracture networks for modelling coupled geomechanical and hydrological behaviour of fractured rocks. *Comput Geotech*. 2017;85:151–176. <https://doi.org/10.1016/j.compgeo.2016.12.024>.
- Tsang YW, Tsang CF, Neretnieks I, Moreno L. Flow and tracer transport in fractured media: a variable aperture channel model and its properties. *Water Resour Res*. 1988;24(12):2049–2060. <https://doi.org/10.1029/WR024i012p02049>.
- Dessirier B, Sharma KM, Pedersen J, Tsang CF, Niemi A. Channel network modeling of flow and transport in fractured rock at the aspö HRL: data-worth analysis for model development, calibration and prediction. *Water Resour Res*. 2023;59(5), e2022WR033816. <https://doi.org/10.1029/2022WR033816>.
- Koudina N, Gonzalez Garcia R, Thovert JF, Adler PM. Permeability of three-dimensional fracture networks. *Phys Rev E*. 1998;57(4):4466–4479. <https://doi.org/10.1103/PhysRevE.57.4466>.
- Lin YC, Yeh HD. An analytical model with a generalized nonlinear water transfer term for the flow in dual-porosity media induced by constant-rate pumping in a leaky fractured aquifer. *Water Resour Res*. 2021;57(8), e2020WR029186. <https://doi.org/10.1029/2020WR029186>.
- Pandey SN, Chaudhuri A, Kelkar S. A coupled thermo-hydro-mechanical modeling of fracture aperture alteration and reservoir deformation during heat extraction from a geothermal reservoir. *Geothermics*. 2017;65:17–31. <https://doi.org/10.1016/j.geothermics.2016.08.006>.
- Salimzadeh S, Paluszny A, Nick HM, Zimmerman RW. A three-dimensional coupled thermo-hydro-mechanical model for deformable fractured geothermal systems. *Geothermics*. 2018;71:212–224. <https://doi.org/10.1016/j.geothermics.2017.09.012>.
- Renard P, Ababou R. Equivalent permeability tensor of heterogeneous media: upscaling methods and criteria (review and analyses). *Geosciences*. 2022;12(7):269. <https://doi.org/10.3390/geosciences12070269>.
- Liu R, Li B, Jiang Y, Huang N. Review: mathematical expressions for estimating equivalent permeability of rock fracture networks. *Hydrogeol J*. 2016;24(7):1623–1649. <https://doi.org/10.1007/s10040-016-1441-8>.
- Oda M. Permeability tensor for discontinuous rock masses. *Geotechnique*. 1985;35(4):483–495. <https://doi.org/10.1680/geot.1985.35.4.483>.
- Roubinet D, de Dreuzy JR, Davy P. Connectivity-consistent mapping method for 2-D discrete fracture networks. *Water Resour Res*. 2010;46(7). <https://doi.org/10.1029/2009WR008302>.
- Svensson U. A continuum representation of fracture networks. Part I: method and basic test cases. *J Hydrol*. 2001;250(1):170–186. [https://doi.org/10.1016/S0022-1694\(01\)00435-8](https://doi.org/10.1016/S0022-1694(01)00435-8).
- Durlöfsky LJ. Numerical calculation of equivalent grid block permeability tensors for heterogeneous porous media. *Water Resour Res*. 1991;27(5):699–708. <https://doi.org/10.1029/91WR00107>.
- Sánchez-Vila X, Girard JP, Carrera J. A synthesis of approaches to upscaling of hydraulic conductivities. *Water Resour Res*. 1995;31(4):867–882. <https://doi.org/10.1029/94WR02754>.
- Karimi-Fard M, Durlöfsky LJ. A general gridding, discretization, and coarsening methodology for modeling flow in porous formations with discrete geological features. *Adv Water Resour*. 2016;96:354–372. <https://doi.org/10.1016/j.advwatres.2016.07.019>.
- Romano V, Bigi S, Carnevale F, et al. Hydraulic characterization of a fault zone from fracture distribution. *J Struct Geol*. 2020;135, 104036. <https://doi.org/10.1016/j.jsg.2020.104036>.
- Sweeney MR, Gable CW, Karra S, Stauffer PH, Pawar RJ, Hyman JD. Upscaled discrete fracture matrix model (UDFM): an octree-refined continuum representation of fractured porous media. *Comput Geosci*. 2020;24(1):293–310. <https://doi.org/10.1007/s10596-019-09921-9>.

33. Sævik PN, Jakobsen M, Lien M, Berre I. Anisotropic effective conductivity in fractured rocks by explicit effective medium methods. *Geophys Prospect*. 2014;62(6):1297–1314. <https://doi.org/10.1111/1365-2478.12173>.
34. Oda M. An equivalent continuum model for coupled stress and fluid flow analysis in jointed rock masses. *Water Resour Res*. 1986;22(13):1845–1856. <https://doi.org/10.1029/WR022i013p01845>.
35. Hui MH, Robin M, Karimi-Fard, Mallison B, Durlafsky LJ. A general modeling framework for simulating complex recovery processes in fractured reservoirs at different resolutions. *SPE J*. 2018;23(2):598–613. <https://doi.org/10.2118/182621-PA>.
36. Zareidarmiyani A, Parisio F, Makhnenko RY, Salarirad H, Vilarrasa V. How equivalent are equivalent porous media? *Geophys Res Lett*. 2021;48(9), e2020GL089163. <https://doi.org/10.1029/2020GL089163>.
37. Neuman SP. Trends, prospects and challenges in quantifying flow and transport through fractured rocks. *Hydrogeol J*. 2005;13(1):124–147. <https://doi.org/10.1007/s10040-004-0397-2>.
38. Matthäi SK, Belayneh M. Fluid flow partitioning between fractures and a permeable rock matrix. *Geophys Res Lett*. 2004;31(7). <https://doi.org/10.1029/2003GL019027>.
39. Aguilar-López JP, Bogaard T, Gerke HH. Dual-permeability model improvements for representation of preferential flow in fractured clays. *Water Resour Res*. 2020;56(8), e2020WR027304. <https://doi.org/10.1029/2020WR027304>.
40. Yoo H, Park S, Xie L, et al. Hydro-mechanical modeling of the first and second hydraulic stimulations in a fractured geothermal reservoir in Pohang, South Korea. *Geothermics*. 2021;89, 101982. <https://doi.org/10.1016/j.geothermics.2020.101982>.
41. Neuman SP. Universal scaling of hydraulic conductivities and dispersivities in geologic media. *Water Resour Res*. 1990;26(8):1749–1758. <https://doi.org/10.1029/WR026i008p01749>.
42. Andrés S, Dentz M, Cueto-Felgueroso L. Multirate mass transfer approach for double-porosity poroelasticity in fractured media. *Water Resour Res*. 2021;57(8), e2021WR029804. <https://doi.org/10.1029/2021WR029804>.
43. Zareidarmiyani A, Salarirad H, Vilarrasa V, Kim KI, Lee J, Min KB. Comparison of numerical codes for coupled thermo-hydro-mechanical simulations of fractured media. *J Rock Mech Geotech Eng*. 2020;12(4):850–865. <https://doi.org/10.1016/j.jrmge.2019.12.016>.
44. Faybishenko B, Benson SM, Gale JE. *Fluid Dynamics in Complex Fractured-Porous Systems*. John Wiley & Sons; 2015.
45. Yoshioka K, Parisio F, Naumov D, Lu R, Kolditz O, Nagel T. Comparative verification of discrete and smeared numerical approaches for the simulation of hydraulic fracturing. *Int J Geomath*. 2019;10(1):13. <https://doi.org/10.1007/s13137-019-0126-6>.
46. Berre I, Doster F, Keilegavlen E. Flow in fractured porous media: a review of conceptual models and discretization approaches. *Transport Porous Media*. 2019;130(1):215–236. <https://doi.org/10.1007/s11242-018-1171-6>.
47. Lepillier B, Yoshioka K, Parisio F, Bakker R, Bruhn D. Variational phase-field modeling of hydraulic fracture interaction with natural fractures and application to enhanced geothermal systems. *J Geophys Res Solid Earth*. 2020;125(7), e2020JB019856. <https://doi.org/10.1029/2020JB019856>.
48. Viswanathan HS, Ajo-Franklin J, Birkholzer JT, et al. From fluid flow to coupled processes in fractured rock: recent advances and new frontiers. *Rev Geophys*. 2022;60(1), e2021RG000744. <https://doi.org/10.1029/2021RG000744>.
49. Joyce S, Hartley L, Applegate D, Hoek J, Jackson P. Multi-scale groundwater flow modeling during temperate climate conditions for the safety assessment of the proposed high-level nuclear waste repository site at Forsmark, Sweden. *Hydrogeol J*. 2014;22(6):1233–1249. <https://doi.org/10.1007/s10040-014-1165-6>.
50. Ji SH, Park KW, Lim DH, Kim C, Kim KS, Dershowitz W. A hybrid modeling approach to evaluate the groundwater flow system at the low- and intermediate-level radioactive waste disposal site in Gyeong-Ju, Korea. *Hydrogeol J*. 2012;20(7):1341–1353. <https://doi.org/10.1007/s10040-012-0875-x>.
51. Jiang J, Younis RM. Hybrid coupled discrete-fracture/matrix and multicontinuum models for unconventional-reservoir simulation. *SPE J*. 2016;21(3):1009–1027. <https://doi.org/10.2118/178430-PA>.
52. Li L, Lee SH. Efficient field-scale simulation of black oil in a naturally fractured reservoir through discrete fracture networks and homogenized media. *SPE Reservoir Eval Eng*. 2008;11(4):750–758. <https://doi.org/10.2118/103901-PA>.
53. Bear J. *Dynamics of fluids in porous media*. Courier Corporation. 1972.
54. Carrera J, Martínez-Landa L. Mixed discrete-continuum models: a summary of experiences in test interpretation and model prediction. *GEOPHYSICAL MONOGRAPH-AMERICAN GEOPHYSICAL UNION*. 2000;122:251–266.
55. Zimmerman RW. Coupling in poroelasticity and thermoelasticity. *Int J Rock Mech Min Sci*. 2000;37(1):79–87. [https://doi.org/10.1016/S1365-1609\(99\)00094-5](https://doi.org/10.1016/S1365-1609(99)00094-5).
56. Olivella S, Gens A. Double structure THM analyses of a heating test in a fractured tuff incorporating intrinsic permeability variations. *Int J Rock Mech Min Sci*. 2005;42(5):667–679. <https://doi.org/10.1016/j.ijrmms.2005.03.007>.
57. Olivella S, Alonso EE. Gas flow through clay barriers. *Geotechnique*. 2008;58(3):157–176. <https://doi.org/10.1680/geot.2008.58.3.157>.
58. Yu Y, Damians IP, Bathurst RJ. Influence of choice of FLAC and PLAXIS interface models on reinforced soil-structure interactions. *Comput Geotech*. 2015;65:164–174. <https://doi.org/10.1016/j.comgeo.2014.12.009>.
59. Puig Damians I, Olivella Pastallé S, Bathurst R, Lloret Moranchó A, Josa Garcia-Tornel A. Modeling soil-facing interface interaction with continuum element methodology. *Frontiers in built environment*. 2022;8, 842495, 1.
60. Olivella S, Gens A, Carrera J, Alonso EE. Numerical formulation for a simulator (CODE BRIGHT) for the coupled analysis of saline media. *Eng Comput*. 1996;13(7):87–112. <https://doi.org/10.1108/02644409610151575>.
61. Olivella S, Carrera J, Gens A, Alonso EE. Nonisothermal multiphase flow of brine and gas through saline media. *Transport Porous Media*. 1994;15(3):271–293. <https://doi.org/10.1007/BF00613282>.
62. Hantush MS. Modification of the theory of leaky aquifers. *Journal of Geophysical Research (1896-1977)*. 1960;65(11):3713–3725. <https://doi.org/10.1029/JZ065i011p03713>.
63. Theis CV. The relation between the lowering of the Piezometric surface and the rate and duration of discharge of a well using ground-water storage. *Eos, Transactions American Geophysical Union*. 1935;16(2):519–524. <https://doi.org/10.1029/TR016i002p00519>.
64. Zareidarmiyani A, Salarirad H, Vilarrasa V, De Simone S, Olivella S. Geomechanical response of fractured reservoirs. *Fluids*. 2018;3(4):70. <https://doi.org/10.3390/fluids3040070>.
65. Meier PM, Serbetto F, Christe F, et al. Results from benchmark testing of zonal isolation borehole completions for multi-stage EGS stimulation in the bedretto underground rock laboratory in Switzerland. *OnePetro*. 2022. <https://doi.org/10.56952/ARMA-2022-0292>.
66. Bröker K, Ma X. Estimating the least principal stress in a granitic rock mass: systematic mini-frac tests and elaborated pressure transient analysis. *Rock Mech Rock Eng*. 2022;55(4):1931–1954. <https://doi.org/10.1007/s00603-021-02743-1>.
67. David C, Nejati M, Geremia D. *On Petrophysical and Geomechanical Properties of Bedretto Granite*. ETH Zurich; 2020.
68. Ma X, Doonechaly NG, Hertrich M, Gischi V, Klee G. Preliminary in situ stress and fracture characterization in the bedretto underground laboratory, Swiss Alps: implications on hydraulic stimulation. In: *Rock Mechanics for Natural Resources and Infrastructure Development*. CRC Press; 2019:1559–1567.
69. Ma X, Hertrich M, Amann F, et al. Multi-disciplinary characterizations of the BedrettoLab – a new underground geoscience research facility. *Solid Earth*. 2022;13(2):301–322. <https://doi.org/10.5194/se-13-301-2022>.
70. Shakas A, Maurer H, Giertzuch PL, et al. Permeability enhancement from a hydraulic stimulation imaged with ground penetrating radar. *Geophys Res Lett*. 2020;47(17), e2020GL088783. <https://doi.org/10.1029/2020GL088783>.
71. Vaezi I, Alcolea A, Meier P, Parisio F, Carrera J, Vilarrasa V. Numerical modeling of hydraulic stimulation of fractured crystalline rock at the bedretto underground laboratory for geosciences and geoenergies. *Int J Rock Mech Min Sci*. 2024;176, 105689. <https://doi.org/10.1016/j.ijrmms.2024.105689>.
72. Boyet A, De Simone S, Ge S, Vilarrasa V. Poroelastic stress relaxation, slip stress transfer and friction weakening controlled post-injection seismicity at the Basel Enhanced Geothermal System. *Commun Earth Environ*. 2023;4(1):1–13. <https://doi.org/10.1038/s43247-023-00764-y>.
73. Kivi IR, Vilarrasa V, Kim KI, Yoo H, Min KB. On the role of poroelastic stressing and pore pressure diffusion in discrete fracture and fault system in triggering post-injection seismicity in enhanced geothermal systems. *Int J Rock Mech Min Sci*. 2024;175, 105673. <https://doi.org/10.1016/j.ijrmms.2024.105673>.
74. Alcolea A, Meier P, Vilarrasa V, Olivella S, Carrera J. Hydromechanical modeling of the hydraulic stimulations in borehole PX2 (Pohang, South Korea). *Geothermics*. 2024;120, 103009. <https://doi.org/10.1016/j.geothermics.2024.103009>.
75. Tangirala SK, Parisio F, Vaezi I, Vilarrasa V. Effectiveness of injection protocols for hydraulic stimulation in enhanced geothermal systems. *Geothermics*. 2024;120, 103018. <https://doi.org/10.1016/j.geothermics.2024.103018>.
76. Vilarrasa V, Makhnenko R, Gheibi S. Geomechanical analysis of the influence of CO2 injection location on fault stability. *J Rock Mech Geotech Eng*. 2016;8(6):805–818. <https://doi.org/10.1016/j.jrmge.2016.06.006>.
77. Park YJ, Lee KK, Kosakowski G, Berkowitz B. Transport behavior in three-dimensional fracture intersections. *Water Resour Res*. 2003;39(8). <https://doi.org/10.1029/2002WR001801>.
78. Li G. Tracer mixing at fracture intersections. *Env Geol*. 2002;42(2):137–144. <https://doi.org/10.1007/s00254-001-0483-x>.
79. Lang PS, Paluszny A, Zimmerman RW. Permeability tensor of three-dimensional fractured porous rock and a comparison to trace map predictions. *J Geophys Res Solid Earth*. 2014;119(8):6288–6307. <https://doi.org/10.1002/2014JB011027>.
80. Garipov TT, Hui MH. Discrete Fracture Modeling approach for simulating coupled thermo-hydro-mechanical effects in fractured reservoirs. *Int J Rock Mech Min Sci*. 2019;122, 104075. <https://doi.org/10.1016/j.ijrmms.2019.104075>.
81. Boyet A, De Simone S, Vilarrasa V. Physics-based modeling to understand and to propose forecasting methods of induced seismicity. *Seismol Res Lett*. 2023;94(6):2666–2678. <https://doi.org/10.1785/0220230109>.